INTERNATIONAL JOURNAL FOR NUMERICAL METHODS IN ENGINEERING, VOL. 40, 269–294 (1997)

A FINITE ELEMENT PERTURBATION METHOD FOR COMPUTING FLUID-INDUCED FORCES ON A CENTRIFUGAL IMPELLER ROTATING AND WHIRLING IN A VOLUTE CASING

J. B. JONKER AND T. G. VAN ESSEN

Faculty of Mechanical Engineering, University of Twente, Enschede, The Netherlands

SUMMARY

A finite element based method has been developed for computing time-averaged fluid-induced radial excitation forces and rotor dynamic forces on a two-dimensional centrifugal impeller rotating and whirling in a volute casing. In this method potential flow theory is used, which implies the assumption of irrotational inviscid flow. In comparison with other analyses of fluid-induced impeller forces, two main features have been included. Firstly, the hydrodynamic interaction between impeller and volute is properly modelled. Secondly, the variation of the width of the volute has been adequately included in the two-dimensional analysis by a modification of the equation of continuity. A regular perturbation method is used to deal with the effects of the whirling motion of the impeller. The excitation forces are calculated from the zeroth-order problem in which the impeller axis is placed at the volute origin. The rotor dynamic forces associated with the whirling motion of the impeller are derived from the first-order solution. The force components, tangential and normal to the whirl orbit, are predicted as functions of the impeller–volute geometry, the flow conditions and the whirl speed ratio. The method is applied to a centrifugal pump experimentally tested at the California Institute of Technology. Comparisons between predictions and experimental data show the capabilities of the proposed method to reproduce the main features of fluid-induced impeller forces in centrifugal pumps.

KEY WORDS: centrifugal pumps; potential fluid flow; unsteady flow; fluid forces; finite element method; perturbation analysis

1. INTRODUCTION

Accurate simulation of pump rotor response and determination of the critical speeds meet with the fundamental problem that the dynamic behaviour of the rotor shaft is significantly affected by fluid-induced forces on the impeller. These forces result from the hydrodynamic interaction between the impeller and the volute. At off-design operation, the static pressure is not constant around the periphery of the impeller and the resulting flow will be unsteady in both the impeller channels and the volute casing. This causes a time-varying radial excitation force on the pump shaft. Forced vibration tests at the California Institute of Technology (CalTech)[1–4] have shown that impellers generate additional forces due to a whirling motion of the impeller shaft. These forces, which are called rotor-dynamic forces, can initiate unstable subsynchronous impeller motion. Rotor dynamic forces on a five-bladed centrifugal impeller (impeller X) in a spiral volute (volute A) have been measured by Jery *et al.*,[4] Adkins[1] and Adkins and Brennen.[2] In these experiments the impeller is forced into a whirling motion in which the impeller centre is made to follow a circular orbit, at a constant angular speed, while the impeller axis remains parallel to the pump centreline. From these

CCC 0029–5981/97/020269–26

Received 24 November 1995
Revised 3 June 1996

measurements two fluid–structure interaction mechanisms have been identified as contributing to the rotor-dynamic forces on the impeller: (1) forces from the discharge-to-suction leakage flow in the varying clearance between the impeller front shroud and the casing wall; (2) forces due to the unsteady flow field within the whirling impeller channels. The latter forces form the subject of this paper.

The analysis of fluid forces on centrifugal pump impellers is very complicated due to the complex behaviour of real fluids and the continuously changing three-dimensional geometry of the impeller–volute configuration. Fortunately, the problem can be simplified while leaving the essentials of the fluid flow model intact. Firstly, it is assumed that the fluid may be considered incompressible when dealing with pumps. Secondly, the main flow in the impeller channels may be assumed to be inviscid and irrotational viewed from a fixed (inertial) reference frame. This is a reasonable assumption for well-designed impellers with backward curved blades in which no flow separation occurs for a broad range of operating conditions. With these assumptions it is possible to compute the fluid-induced forces on the basis of potential flow theory.

A number of authors have contributed to solutions of potential flow in centrifugal pumps in order to study the fluid-induced forces on a rotating impeller in whirling motion. Ohashi and Shoij[5] developed two-dimensional potential flow models based on the method of singularities. Tsujimoto *et al.*[6] similarly used a vortex distribution to model the volute, including the unsteady vortex distribution. The impeller was treated as an actuator disk, with the impeller flow being perfectly guided by the blades. Adkins and Brennen[1, 2] developed quasi-one-dimensional models for the flow through both the impeller and the volute. The flow in the impeller was assumed to follow a spiral path with a prescribed inclination whereas a bulk flow description of the volute flow was used. The models were then combined by matching the pressures and velocities at the impeller outlet. In none of these studies a solution of the unsteady potential flow equations has been developed for the actual three-dimensional impeller–volute configuration. Correct modelling of forces in centrifugal pumps requires accurate geometrical modelling of the impeller and the volute. A number of authors have developed finite element models for this problem. The main attributes of the finite element method are its ease in handling the very complex pump geometry and its ability to naturally incorporate differential-type boundary conditions. Liu *et al.*[7] developed a linear perturbation model for determining the hydrodynamic mass of a mixed-flow impeller of a nuclear pump. The undisturbed potential flow field was computed by using a finite element representation of the three-dimensional geometry of the pump. However, the relative flow field in the impeller was assumed to be steady in this model. Recently Wood and Thaker[8] presented a two-dimensional finite element model of a whirling centrifugal impeller in a volute. The unsteady flow effects due to the whirling motion of the impeller were incorporated through the boundary conditions at the inlet and on the blade surfaces. Computed forces and the stiffness matrix were compared with experimental results of the CalTech pump.[1] The increase of the volute width in the axial direction was however not included in the two-dimensional calculations which made a comparison to test results difficult. The experimental stiffness matrix showed non-zero components for the zero whirl case whereas the calculations showed zero components at zero whirl. This means that destabilizing effects cannot be simulated by this model.

The method presented in this paper uses a two-dimensional finite element model developed by Badie *et al.*[9] to calculate the unsteady potential flow in a centrifugal pump, including vortex sheets downstream of the blades by using a linearized vortex distribution. The width variation of the three-dimensional volute profile is taken into account in the two-dimensional model by adapting the equation of continuity. The computational domain is separated into two regions. One region contains the impeller and the other the volute. The corresponding meshes are matched by a

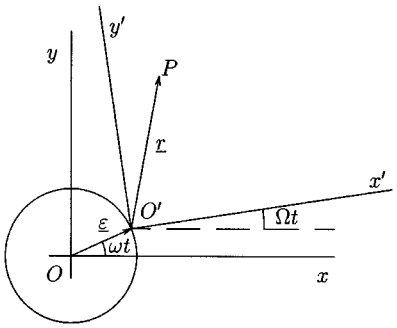

Figure 1. Centrifugal impeller in whirling condition

sliding interface consisting of connect elements between the meshes that are fixed in the impeller and the volute. A control volume formulation is used to calculate the time average forces acting on the impeller.

The model is then extended in order to obtain the fluid force perturbations that are caused by the whirling motion of the impeller. A regular perturbation analysis of the flow governing equations is used to deal with the effects of the whirling motion of the impeller. It is assumed that the impeller whirls on a circular orbit with constant whirl speed. The method is tested by comparing calculated fluid forces with experimental results of Arndt and Franz.[3] A full description of this method is given by van Essen.[10]

2. GOVERNING EQUATIONS

2.1. Frames of reference

The plane motion of the impeller in the whirling condition is illustrated in Figure 1. The position of the impeller centre O' relative to the geometric volute centre O in the absolute (inertial) co-ordinate system (x, y) is given by the whirl orbit vector $\boldsymbol{\varepsilon}$.

The relative co-ordinate system (x', y') is fixed to the impeller with origin O'. The impeller rotates at constant angular velocity $\boldsymbol{\Omega}$ about the machine axis of rotation through O'. The angular speed determines the angle Ωt between the co-ordinate axis $O'x'$ and the horizontal Ox at time t.

Let $\mathbf{w}$ be the velocity of the fluid relative to the moving coordinate system (x', y'). Then the absolute velocity $\mathbf{v}$ at the point P on the impeller, whose position vector referred to O' is $\mathbf{r}$, can be written as

$$\mathbf{v} = \mathbf{w} + \dot{\boldsymbol{\varepsilon}} + \boldsymbol{\Omega} \times \mathbf{r} \tag{1}$$

where $\dot{\boldsymbol{\varepsilon}}$ represents the whirl orbit velocity of the impeller centre O' relative to the geometric volute centre O. In the case of a whirling motion with a circular orbit with radius ε we have

$$\boldsymbol{\varepsilon} = \varepsilon \mathbf{e} \tag{2}$$

and

$$\dot{\boldsymbol{\varepsilon}} = \varepsilon(\boldsymbol{\omega} \times \mathbf{e}) \tag{3}$$

where $\mathbf{e}$ is a unit vector in the direction of $\boldsymbol{\varepsilon}$ and $\boldsymbol{\omega}$ is the angular velocity of the whirling motion.

2.2. Potential flow equation

The absolute velocity $\mathbf{v}$ is related to a time-dependent potential ϕ by

$$\mathbf{v} = \boldsymbol{\nabla}\phi \tag{4}$$

where $\boldsymbol{\nabla}$ represents the gradient operator. Since the fluid we are dealing with is incompressible the absolute velocity field obeys the equation of continuity, which for a two-dimensional flow can be written by the equation

$$\boldsymbol{\nabla} \cdot (b\mathbf{v}) = 0 \tag{5}$$

where b is a function which represents the width of the impeller and the volute casing. Substitution of equation (4) in equation (5) yields the potential equation

$$\boldsymbol{\nabla} \cdot (b\boldsymbol{\nabla}\phi) = 0 \tag{6}$$

This is an elliptic type of equation. Boundary conditions appropriate for the solution of equation (6) are either to specify ϕ or to specify the normal derivative $\partial\phi/\partial n$ around a closed region.

2.3. Pressure equations

The pressure field can be obtained from the unsteady Bernoulli equation[11]

$$\frac{\partial\phi}{\partial t} + \frac{1}{2}(\mathbf{v} \cdot \mathbf{v}) + \frac{p}{\rho} = c(t) \tag{7}$$

where p is the pressure, ρ the density and c the Bernoulli constant. Note that the local time derivative $\partial\phi/\partial t$ is calculated by varying t only and therefore refers to a fixed point in the absolute co-ordinate system. The unsteadiness of the flow is introduced through the rotation of the impeller blades with respect to the volute casing. For calculation of the unsteady flow field within the impeller channels it is advantageous to calculate the local time derivative with respect to the relative co-ordinate system. The local time derivatives in the absolute and relative co-ordinate system are related by the identity (see Appendix I)

$$\frac{\partial\phi}{\partial t} = \left.\frac{\partial\phi}{\partial t}\right|' - (\mathbf{v} - \mathbf{w}) \cdot \boldsymbol{\nabla}\phi \tag{8}$$

where the superscript $'$ indicates that the derivative is taken in the relative co-ordinate system. Then by use of equation (1) the Bernoulli equation (7) for the potential ϕ, referred to the relative co-ordinate system, becomes

$$\left.\frac{\partial\phi}{\partial t}\right|' + \frac{1}{2}(\mathbf{v} \cdot \mathbf{v}) - (\dot{\boldsymbol{\varepsilon}} + \boldsymbol{\Omega} \times \mathbf{r}) \cdot \mathbf{v} + \frac{p}{\rho} = c(t) \tag{9}$$

2.4. Vortex distribution downstream of the impeller blades

One of the major problems of potential flow theory to the solution of the flow around the impeller blades is the determination of the circulation generated by the viscous shear layer at the trailing edges. Kelvin's circulation theorem states that for an inviscid and incompressible flow the circulation of the potential flow around a blade and its wake is a conserved quantity, i.e.

$$\frac{\mathrm{D}\Gamma}{\mathrm{D}t} = 0 \tag{10}$$

where Γ is the circulation around a closed curve S with unit vector $\mathbf{s}$ tangential to S,

$$\Gamma = \oint_S \mathbf{v} \cdot \mathrm{d}\mathbf{s} \tag{11}$$

When the impeller is rotating in the volute casing, the circulation around the blades is changing continuously with time according to the unsteady Kutta condition that velocities and pressures remain finite at the trailing edge. Equation (10) then implies that this change is accompanied by vortex shedding downstream of the blades. In potential flow analyses, circulation and vortex shedding are introduced by potential discontinuities on suitable slit lines and wake curves (which are mathematical cuts) in the computational domain.[11] To derive the equations governing the potential jumps on the wake curves, we consider a blade with a vortex wake extending from the trailing edge. The wake is assumed to be thin enough that it can be concentrated at a curve with two sides: the upper side and the lower side. We introduce the following symbols: ϕ^+, the limit of the velocity potential when the wake is approached from the upper side of the wake curve; ϕ^-, the limit of the velocity potential when the wake is approached from the lower side of the wake curve. On this curve the potential jump must be such that the pressure field and the velocity component normal to the wake curve are continuous, i.e.,

$$p^+ = p^-$$

and

$$v_n^+ = v_n^-$$

From the Bernoulli equation (7) it then follows that

$$\frac{\partial}{\partial t}(\phi^+ - \phi^-) + \frac{1}{2}\left((v_s^+)^2 - (v_s^-)^2\right) = 0 \tag{12}$$

In the present paper a linearized vortex description is employed in which the location of the wake curve and the mainstream velocity along the wake curve are determined from a quasi-unsteady analysis in which the unsteady wakes are neglected.[12] Since equation (6) is linear, its solution can be divided into two separate parts,

$$\phi = \bar{\phi} + \tilde{\phi} \quad (\,|\nabla\tilde{\phi}| \ll |\nabla\bar{\phi}|\,) \tag{13}$$

where $\tilde{\phi}$ is the perturbation potential caused by the existence of a vortex sheet and $\bar{\phi}$ is the potential obtained from a quasi-unsteady analysis. Using this relation we then have, after linearization,

$$\frac{\partial}{\partial t}(\phi^+ - \phi^-) + \bar{v}_s \frac{\partial}{\partial s}(\phi^+ - \phi^-) = 0 \tag{14}$$

where

$$\bar{v}_s = \frac{1}{2}\frac{\partial}{\partial s}(\bar{\phi}^+ + \bar{\phi}^-) \tag{15}$$

is the mainstream velocity along the wake curve. Equation (14) can be transformed to the relative co-ordinate system by using identity (8) and equation (1). Then equation (14) for the potential, referred to the relative co-ordinate system, becomes

$$\left.\frac{\partial}{\partial t}\right|' (\phi^+ - \phi^-) + \bar{w}_s \frac{\partial}{\partial s}(\phi^+ - \phi^-) = 0 \tag{16}$$

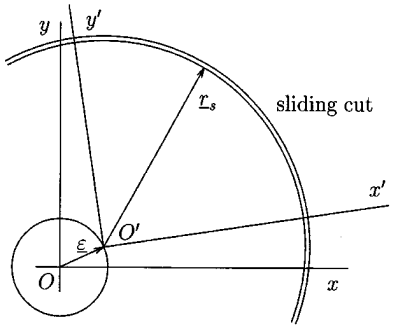

Figure 2. Rotor–stator interface for a whirling impeller

where $\overline{w}_s$ represents the relative mainstream velocity along the wake curve. Equations (14) and (16) describe the vortex distribution of the wake, i.e. the potential jump distribution as a function of time t and position s along a wake curve in the absolute and relative co-ordinate system, respectively.

3. COMPUTATIONAL DOMAIN

3.1. Coupling conditions between rotor and stator region

The numerical calculation of the vortex distribution along the wake curves requires the solution of equation (6) for a sequence of impeller–volute configurations corresponding to impeller positions at various times through one complete pitch cycle. This would lead to problems due to moving boundaries if the computational domain were to be regarded from one co-ordinate system. The most natural approach to this problem is to split the computational domain into two parts. One part containing the impeller is considered from the moving co-ordinate system (x', y') fixed to the impeller whereas the stator part is treated in the absolute (inertial) co-ordinate system (x, y) fixed to the volute casing. The interface between the two parts is modelled as two coinciding circles which form a sliding cut in the computational domain. The central point of the circles is located at the impeller centre O' as shown in Figure 2. Let $\mathbf{r}_s$ be the radius vector of a point on the sliding cut relative to the impeller centre O' which is positioned relative to O by the whirl orbit vector $\boldsymbol{\varepsilon}$. Then the coupling conditions for the velocity potential become

$$\phi'(\mathbf{r}_s) = \phi(\mathbf{r}_s + \boldsymbol{\varepsilon}) \tag{17a}$$

$$\left|\frac{\partial \phi'}{\partial n}\right|_{\mathbf{r}_s} = -\left|\frac{\partial \phi}{\partial n}\right|_{\mathbf{r}_s+\boldsymbol{\varepsilon}} \tag{17b}$$

where superscript $'$ refers to the rotor region. The direction $\mathbf{n}$ is an outward normal to the respective domains.

3.2. Boundary conditions

Figure 3 shows the computational domain of a centrifugal pump. The impeller is equipped with Z blades (in the figure there are five blades without thickness). The flow is emitted from the origin of the volute centre and enters the impeller region through a circular inlet. The boundary

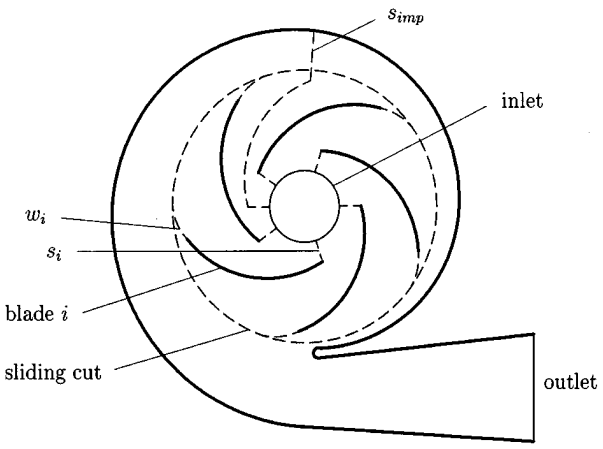

Figure 3. Computational domain

conditions which must be satisfied at each time are

$$\frac{\partial \phi}{\partial n} = 0 \quad \text{on the volute wall} \tag{18a}$$

$$\frac{\partial \phi}{\partial n} = \pm(\boldsymbol{\Omega} \times \mathbf{r} + \dot{\boldsymbol{\varepsilon}}) \cdot \mathbf{n} \quad \text{at the blade surfaces} \tag{18b}$$

$$\frac{\partial \phi}{\partial n} = -\frac{Q}{b l_{\text{in}}} \quad \text{at the impeller inlet} \tag{18c}$$

$$\frac{\partial \phi}{\partial n} = \frac{Q}{b l_{\text{out}}} \quad \text{at the volute outlet} \tag{18d}$$

$$\phi = 0 \quad \text{at a point somewhere in the geometry} \tag{18e}$$

Here l_{in} and l_{out} are the lengths of the inlet and outlet, respectively, n is the outward normal and Q is the volume flow rate. The sign for the boundary conditions on the blades is dependent upon the side of the blade considered. Note that the eccentric location of the impeller inlet in the boundary condition (18c) is neglected. The reason for this is that computations with an additional sliding cut at the inlet region appeared to have little effect on the results.[10]

3.3. Slit lines and wake curves

In order to make the region simply connected, cuts have to be made in the domain. Circulation of the flow around the blades and wakes is realized by introducing potential jumps on slit lines (in the figure denoted by s_i) and wake curves (denoted by w_i in the figure). To each blade there belongs a slit line s_i from the leading edge of blade i to the inlet boundary of the domain and on which a jump in the potential equal to Γ_i can be realized. Note that Γ_i represents the circulation around blade i and its wake, i.e.,

$$\Gamma_i = (\Gamma_b)_i + (\Gamma_w)_i \tag{19}$$

where $(\Gamma_b)_i$ is the blade circulation and $(\Gamma_w)_i$ the wake circulation of blade i. An extra cut s_{imp} from the inlet boundary to the volute boundary must be introduced to impose the impeller

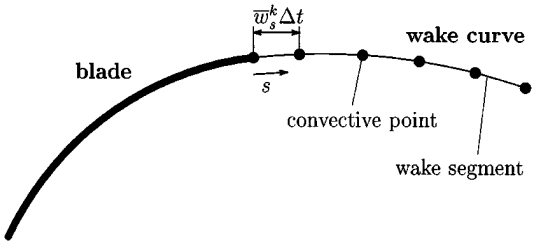

Figure 4. Vortex representation of a blade

circulation Γ_{out}. This circulation can be determined from the relation

$$\Gamma_{\text{out}} = \Gamma_{\text{in}} + \sum_{i=1}^{Z} \Gamma_i \tag{20}$$

where Γ_{in} represents the circulation of the inlet flow. From the above-mentioned considerations the following jump conditions must be imposed at the slit lines:

$$\begin{cases} \phi^+ - \phi^- = \Gamma_i \\ \dfrac{\partial \phi^+}{\partial n} = -\dfrac{\partial \phi^-}{\partial n} \end{cases} \quad \text{across slit lines } s_i \tag{21a}$$

$$\begin{cases} \phi^+ - \phi^- = \Gamma_{\text{out}} \\ \dfrac{\partial \phi^+}{\partial n} = -\dfrac{\partial \phi^-}{\partial n} \end{cases} \quad \text{across slit line } s_{\text{imp}} \tag{21b}$$

A discrete vortex model[9] of the continuous vortex sheet is introduced by a vortex wake curve consisting of vortex segments as shown in Figure 4.

The vortex segments are bounded by convective points which move with the averaged relative velocity $\overline{w}_s$ along the wake curves. The positions of the convective points generally do not coincide with the nodal points on the wake curve of elements adjacent to the wake curve. Therefore the averaged velocity $\overline{w}_s$ is linearly interpolated from corresponding nodal points on the wake curve. At each time step newly formed vortices are shed in the wake and are convected downstream with the main flow as described by equation (16). The circulation of the latest vortex segment k at the trailing edge Γ_w^k (i.e. the first wake segment downstream of a blade) is equal to the vorticity shed during the time interval $(k-1)\Delta t < t < k\Delta t$; thus

$$\Gamma_w^k = \int_{(k-1)\Delta t}^{k\Delta t} \gamma_w^k \overline{w}_s^k \, \mathrm{d}t \tag{22}$$

where γ_w^k is the vorticity distribution of segment k defined as

$$\gamma_w^k = \frac{\partial}{\partial s}(\phi^+ - \phi^-)^k \tag{23}$$

For each segment a linear distribution of the velocity potential is imposed. In this way the jump in the velocity potential on wake curve w_i is represented by a piecewise linear and continuous function $(f_w)_i$. The jump conditions to be imposed in the wake curves are

$$\begin{cases} \phi^+ - \phi^- = (f_w)_i \\ \dfrac{\partial \phi^+}{\partial n} = -\dfrac{\partial \phi^-}{\partial n} \end{cases} \quad \text{across wake curve } w_i \tag{24}$$

The functions $(f_w)_i$ are linearly interpolated from the convective points to corresponding nodal points on the wake curve. Only the part of the wake in the impeller region is modelled which has the most significant effect on the determination of the Kutta condition at the trailing edge.

4. PERTURBATION METHOD

The coupling conditions (17) at the sliding cut do not allow for a direct implementation in a finite element model since for the case of a whirling impeller motion the sliding cut moves eccentrically in the stator region. However, for small amplitudes of the whirling motion a regular perturbation analysis can be employed to deal with the effects of the eccentric motion of the impeller. We will make the assumption that the flow field can be composed of the flow associated with the centric rotation of the impeller and a perturbation flow due to the whirling motion of the impeller. Therefore

$$\mathbf{v} = \mathbf{v}_0 + \frac{\varepsilon}{r_2}\mathbf{v}_1 + O\left(\left(\frac{\varepsilon}{r_2}\right)^2\right) \tag{25a}$$

$$p = p_0 + \frac{\varepsilon}{r_2}p_1 + O\left(\left(\frac{\varepsilon}{r_2}\right)^2\right) \tag{25b}$$

where the subscripts 0 and 1 denote the zeroth-order and first-order approximation, respectively, and r_2 is the impeller discharge radius. Substituting these relations into the equations from Sections 2 and 3 and equating coefficients of equal powers of $(\varepsilon/r_2)^0$ and $(\varepsilon/r_2)^1$ we derive a system of zeroth-order and first-order equations which both can be solved for a centric position of the impeller.

4.1. Zeroth-order equations

(a) For v_0 and ϕ_0

$$\mathbf{v}_0 = \mathbf{w}_0 + \boldsymbol{\Omega} \times \mathbf{r} \tag{26}$$

$$\mathbf{v}_0 = \boldsymbol{\nabla}\phi_0 \tag{27}$$

$$\boldsymbol{\nabla} \cdot b\boldsymbol{\nabla}\phi_0 = 0 \tag{28}$$

subject to the following boundary and coupling conditions:

$$\frac{\partial\phi_0}{\partial n} = 0 \quad \text{on the volute} \tag{29a}$$

$$\frac{\partial\phi_0}{\partial n} = \pm(\boldsymbol{\Omega} \times \mathbf{r}) \cdot \mathbf{n} \quad \text{at the blade surface} \tag{29b}$$

$$\frac{\partial\phi_0}{\partial n} = -\frac{Q}{bl_{\text{in}}} \quad \text{at the impeller inlet} \tag{29c}$$

$$\frac{\partial\phi_0}{\partial n} = \frac{Q}{bl_{\text{out}}} \quad \text{at the volute outlet} \tag{29d}$$

$$\begin{cases} \phi_0^+ - \phi_0^- = (\Gamma_0)_i \\ \dfrac{\partial \phi_0^+}{\partial n} = -\dfrac{\partial \phi_0^-}{\partial n} \end{cases} \quad \text{across slit line } s_i \tag{29e}$$

$$\begin{cases} \phi_0^+ - \phi_0^- = (\Gamma_0)_{\text{out}} \\ \dfrac{\partial \phi_0^+}{\partial n} = -\dfrac{\partial \phi_0^-}{\partial n} \end{cases} \quad \text{across slit line } s_{\text{imp}} \tag{29f}$$

$$\begin{cases} \phi_0^+ - \phi_0^- = (f_{w0})_i \\ \dfrac{\partial \phi_0^+}{\partial n} = -\dfrac{\partial \phi_0^-}{\partial n} \end{cases} \quad \text{across wake curve } w_i \tag{29g}$$

$$\begin{cases} \phi_0' = \phi_0 \\ \dfrac{\partial \phi_0'}{\partial n} = -\dfrac{\partial \phi_0}{\partial n} \end{cases} \quad \text{at the sliding cut} \tag{29h}$$

(b) Bernoulli equations,

$$\left.\frac{\partial \phi_0}{\partial t}\right|' + \frac{1}{2}(\mathbf{v}_0 \cdot \mathbf{v}_0) - (\boldsymbol{\Omega} \times \mathbf{r}) \cdot \mathbf{v}_0 + \frac{p_0}{\rho} = c(t) \quad \text{(rotor region)} \tag{30}$$

$$\frac{\partial \phi_0}{\partial t} + \frac{1}{2}(\mathbf{v}_0 \cdot \mathbf{v}_0) + \frac{p_0}{\rho} = c(t) \quad \text{(stator region)} \tag{31}$$

(c) Vortex distribution downstream the impeller blades,

$$\left.\frac{\partial f_{w0}}{\partial t}\right|' + \overline{w}_{0s} \frac{\partial f_{w0}}{\partial s} = 0 \tag{32}$$

4.2. First-order equations

(a) For $\mathbf{v}_1$ and ϕ_1,

$$\mathbf{v}_1 = \mathbf{w}_1 + r_2(\boldsymbol{\omega} \times \mathbf{e}) \tag{33}$$

$$\mathbf{v}_1 = \boldsymbol{\nabla} \phi_1 \tag{34}$$

$$\boldsymbol{\nabla} \cdot b \boldsymbol{\nabla} \phi_1 = 0 \tag{35}$$

subject to the following boundary and coupling conditions:

$$\frac{\partial \phi_1}{\partial n} = 0 \quad \text{on the volute} \tag{36a}$$

$$\frac{\partial \phi_1}{\partial n} = \pm r_2(\boldsymbol{\omega} \times \mathbf{e}) \cdot \mathbf{n} \quad \text{at the blade surface} \tag{36b}$$

$$\frac{\partial \phi_1}{\partial n} = 0 \quad \text{at the impeller inlet} \tag{36c}$$

$$\frac{\partial \phi_1}{\partial n} = 0 \quad \text{at the volute outlet} \tag{36d}$$

$$\begin{cases} \phi_1^+ - \phi_1^- = (\Gamma_1)_i \\ \dfrac{\partial \phi_1^+}{\partial n} = -\dfrac{\partial \phi_1^-}{\partial n} \end{cases} \quad \text{across slit line } s_i \tag{36e}$$

$$\begin{cases} \phi_1^+ - \phi_1^- = (\Gamma_1)_{\text{out}} \\ \dfrac{\partial \phi_1^+}{\partial n} = \dfrac{\partial \phi_1^-}{\partial n} \end{cases} \quad \text{across slit line } s_{\text{imp}} \tag{36f}$$

$$\begin{cases} \phi_1^+ - \phi_1^- = (f_{w1})_i \\ \dfrac{\partial \phi_1^+}{\partial n} = -\dfrac{\partial \phi_1^-}{\partial n} \end{cases} \quad \text{across wake curve } w_i \tag{36g}$$

$$\begin{cases} \phi_1' = \phi_1 + r_2 \nabla \phi_0 \cdot \mathbf{e} \\ \dfrac{\partial \phi_1'}{\partial n} = -\dfrac{\partial \phi_1}{\partial n} + r_2 \nabla (\nabla \phi_0 \cdot \mathbf{e}) \cdot \mathbf{n} \end{cases} \quad \text{at the sliding cut} \tag{36h}$$

(b) Bernoulli equations,

$$\left. \frac{\partial \phi_1}{\partial t} \right|' + (\mathbf{v}_0 \cdot \mathbf{v}_1) - r_2(\boldsymbol{\omega} \times \mathbf{e}) \cdot \mathbf{v}_0 - (\Omega \times \mathbf{r}) \cdot \mathbf{v}_1 + \frac{p_1}{\rho} = 0 \quad \text{(rotor region)} \tag{37}$$

$$\frac{\partial \phi_1}{\partial t} + (\mathbf{v}_0 \cdot \mathbf{v}_1) + \frac{p_1}{\rho} = 0 \quad \text{(stator region)} \tag{38}$$

(c) Vortex distribution downstream the impeller blades,

$$\left. \frac{\partial f_{w1}}{\partial t} \right|' + \overline{w}_{0s} \frac{\partial f_{w1}}{\partial s} = -\overline{w}_{1s} \frac{\partial f_{w0}}{\partial s} \tag{39}$$

The zeroth-order potential solution acts upon the first-order solution by the coupling conditions at the sliding cut, see equation (36h). Equation (36h) is derived from the coupling conditions of equations (17). The first-order pressure field is affected by the term $\mathbf{v}_0 \cdot \mathbf{v}_1$ and the first-order wake is influenced by the zeroth-order wake through the right-hand term in equation (39).

5. MODELLING OF ROTOR–STATOR INTERACTION

In case of a centric position of the impeller, the sliding cut between the rotor and stator region is located symmetrical with respect to the geometric volute centre O. The sliding cut is modelled as two sliding circles corresponding to the two regions. The nodal points on these circles, which are distributed equidistantly, are connected to each other for a specific time step by means of so-called mesh-connect elements. These connections have to change with time according to the displacement of the rotor with respect to the stator. Figure 5 illustrates the above-mentioned idea. The rotor and stator meshes consist of triangular quadratic elements. The mesh-connect elements are indicated by dashed lines representing a zero potential jump and those indicated by dotted lines representing a finite potential jump between the nodes connected. To define all the connections in a unique way, the starting point is as shown for time $t = t^1$. At another instant, say $t = t^2$, the connections have to be changed accordingly as shown in the figure.

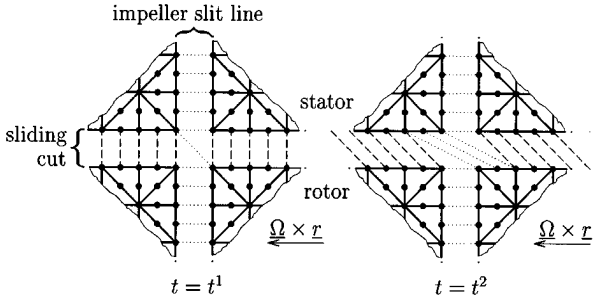

Figure 5. Use of the sliding cut

Within the presented approach, numerical solutions of equation (6) can be generated for a sequence of impeller–volute configurations corresponding to impeller positions at discrete times through one complete pitch cycle. If N_e is the total number of elements along the sliding cut, then the time difference associated with a mesh step is defined as

$$\Delta t = t^k - t^{k-1} = \frac{2\pi}{\Omega N_e} \tag{40}$$

Thus the accuracy of the above rotor–stator interaction scheme depends on the number of elements on the sliding cut.

6. KUTTA CONDITIONS

The strength of the newly formed vortices is determined by satisfying the Kutta condition at each instant. The method to be used to determine the associated circulations is based on the superposition principle.[13] For each time step the velocity potential ϕ_0^k is split into $(Z+1)$ subpotentials according to

$$\phi_0^k = \phi_{0r}^k + \sum_{i=1}^{Z} \left(\Gamma_{w0}^k\right)_i \phi_i \tag{41}$$

where ϕ_{0r}^k is the velocity potential developed up to the actual time excluding the newly formed vortices, $\left(\Gamma_{w0}^k\right)_i$ are the Z unknown circulations of the newly formed wake segments to be calculated and ϕ_i is the potential due to a linear unit vortex distribution on the latest segment of the wake belonging to blade number i. By a unit vortex distribution we mean a potential jump on the vortex wake which has the value unity at the blade trailing edge and decreases linearly to zero at position $\overline{w}_{0s}^k \Delta t$. For this distribution the circulation Γ_{w0}^k is equal to the change of the potential jump at the trailing edge, i.e.

$$\Gamma_{w0}^k = (\phi_0^+ - \phi_0^-)_i^k \tag{42}$$

To satisfy the Kutta condition at the trailing edges, it is necessary that the following relation holds at each instant,

$$\left.\frac{\partial \phi_0}{\partial n}\right|_{\text{tip i}} = (\mathbf{\Omega} \times \mathbf{r}_{\text{tip i}}) \cdot \mathbf{n}_{\text{tip i}} \tag{43}$$

where the subscript tip is used to indicate the trailing edge of the blades. By imposing this condition at each of the Z trailing edges and solving the subpotentials of equation (41) separately,

the following system of linear equations is obtained for the circulation values of the newly formed vortex segments:

$$\begin{bmatrix} \left.\frac{\partial \phi_1^k}{\partial n}\right|_{\text{tip } 1} & \cdots & \left.\frac{\partial \phi_Z^k}{\partial n}\right|_{\text{tip } 1} \\ \vdots & & \vdots \\ \left.\frac{\partial \phi_1^k}{\partial n}\right|_{\text{tip } Z} & \cdots & \left.\frac{\partial \phi_Z^k}{\partial n}\right|_{\text{tip } Z} \end{bmatrix} \begin{bmatrix} (\Gamma_{w0}^k)_1 \\ \vdots \\ (\Gamma_{w0}^k)_Z \end{bmatrix} + \begin{bmatrix} \left.\frac{\partial \phi_{0r}^k}{\partial n}\right|_{\text{tip } 1} \\ \vdots \\ \left.\frac{\partial \phi_{0r}^k}{\partial n}\right|_{\text{tip } Z} \end{bmatrix}$$

$$= \begin{bmatrix} (\boldsymbol{\Omega} \times \mathbf{r}) \cdot \mathbf{n}|_{\text{tip } 1} \\ \vdots \\ (\boldsymbol{\Omega} \times \mathbf{r}) \cdot \mathbf{n}|_{\text{tip } Z} \end{bmatrix} \tag{44}$$

The components $\partial \phi_i^k / \partial n$ have to be computed only once for each impeller position, whereas the components $\partial \phi_{0r}^k / \partial n$ must be computed again at each time step. The unsteady solution of the zeroth-order flow field at successive intervals of time t^k ($t^0 = 0$, $k = 1, 2, \ldots$) is attained as follows. At time $t^0 = 0$ the computation is started from a zero potential jump distribution along the wake curves. Let a downstream vortex distribution be developed at time t^{k-1} as shown in Figure 6(a). Then the computation proceeds with two substeps comprising a full time step.

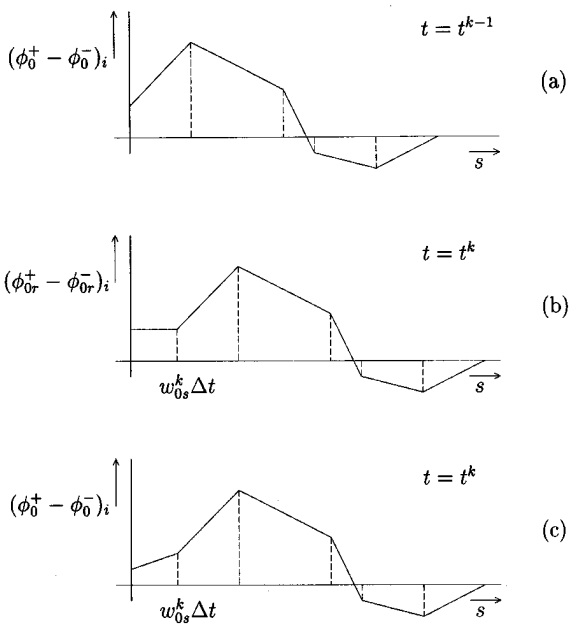

Figure 6. Potential jump distribution along wake curve w_i

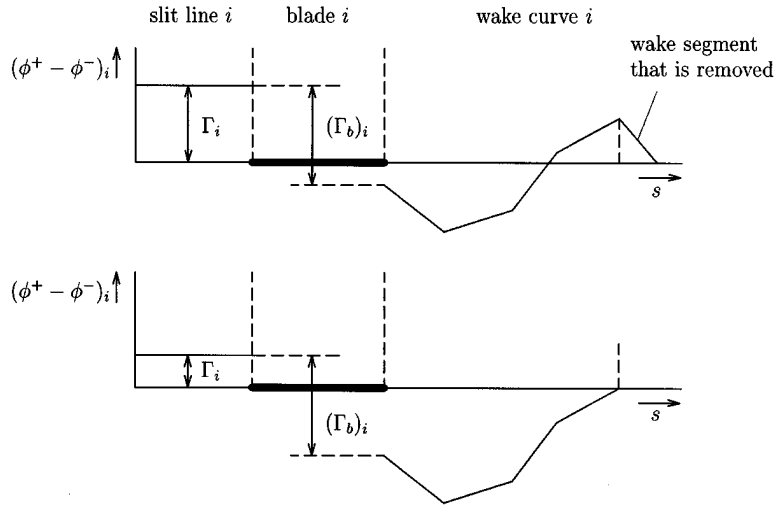

Figure 7. Adaption of the wake distribution along wake curve w_i after segment

(1) Convection step: all vortex segments are convected along the wake curves using equation (32). A straight-line wake segment of length $\overline{w}_{0s}^k \Delta t$ and zero circulation is attached to the trailing edge as shown in Figure 6(b).

(2) Configuration step: the rotor–stator configuration is adapted by a mesh step. The wake distribution that resulted from the convection step is used for the computation of the subpotential ϕ_{0r}^k at time $t = t^k$ by using equation (28) and the components $\partial\phi_{0r}^k/\partial n$ are calculated according to (27). Then the circulation values $\left(\Gamma_{w0}^k\right)_i$ of the newly formed vortex segments at time $t = t^k$ are calculated using equations (44), such that the Kutta conditions are satisfied for the time step considered. The newly formed wake segments are added to the wake curve, as shown in Figure 6(c). According to equation (42) the change of the potential jump at each blade trailing edge is equal to the change in circulation around the blade and its wake between times t^{k-1} and t^k. Once $\left(\Gamma_{w0}^k\right)_i$ $(i = 1, \ldots, Z)$ are known, the velocity potential ϕ_0^k is calculated again using equation (28).

In this way a downstream wake of vortex segments is formed from the vorticity shed at earlier times, which is assumed to be concentrated into a discrete vortex distribution convected along the wake curves. The wake segments that reach the end of the wake curve near the sliding cut are removed. This removal of wake segment must be treated carefully in order to avoid a physically unrealistic velocity distribution near the end of the wake curve. Therefore, a wake segment, that would pass the end of the wake curve, is removed before the convection step is executed. The remaining wake distribution is adapted until a zero potential jump has been achieved at the end of the wake curve. The removal of a wake segment is illustrated in Figure 7. Note that during the adaption of the wake distribution, the blade circulation $(\Gamma_b)_i$ remains unchanged.

Since we seek for a periodic solution with the blade passing frequency $(1/T_0)$, the configuration of the vortex distribution must ultimately show a periodic behaviour with the same frequency. The above procedure is repeated until $\phi_0(t)$ and $\phi_0(t - T_0)$ have converged to the desired accuracy. The convergence criterion to be met verifies this periodicity of the flow. The following criterion

is used:

$$\max |\phi_0(t) - \phi_0(t - T_0)| < \mu, \quad t \in [jT_0, (j+1)T_0],\ j = 0, 1, 2, \ldots, m \tag{45}$$

where μ is a user-defined tolerance, T_0 the time period of the blade passing frequency and m the maximum number of iterations. After a converged zeroth-order solution has been achieved, the velocity distribution is calculated from equation (27).

A similar procedure is used for the calculation of the downstream wake distribution of the first-order flow field. For each time step the velocity potential ϕ_1^k is split into $(Z + 1)$ subpotentials according to

$$\phi_1^k = \phi_{1r}^k + \sum_{i=1}^{Z} \left(\Gamma_{w1}^k\right)_i \phi_i \tag{46}$$

where ϕ_{1r}^k is the velocity potential developed up to the actual time including the newly formed vortices and $\left(\Gamma_{w1}^k\right)_i$ are the Z unknown circulations of the newly formed wake segments to be calculated from the Kutta condition at the blade trailing edges

$$\left.\frac{\partial \phi_1}{\partial n}\right|_{\text{tip i}} = r_2(\boldsymbol{\omega} \times \mathbf{e}) \cdot \mathbf{n}_{\text{tip } i} \tag{47}$$

By imposing this condition at each of the Z trailing edges and solving the subpotentials of equation (46) separately, a system of linear equations is obtained for the circulation values $(\Gamma_{w1}^k)_i$

$$\begin{bmatrix} \left.\frac{\partial \phi_1^k}{\partial n}\right|_{\text{tip } 1} & \cdots & \left.\frac{\partial \phi_Z^k}{\partial n}\right|_{\text{tip } 1} \\ \vdots & \ddots & \vdots \\ \left.\frac{\partial \phi_1^k}{\partial n}\right|_{\text{tip } Z} & \cdots & \left.\frac{\partial \phi_Z^k}{\partial n}\right|_{\text{tip } Z} \end{bmatrix} \begin{bmatrix} \left(\Gamma_{w1}^k\right)_1 \\ \vdots \\ \left(\Gamma_{w1}^k\right)_Z \end{bmatrix} + \begin{bmatrix} \left.\frac{\partial \phi_{1r}^k}{\partial n}\right|_{\text{tip } 1} \\ \vdots \\ \left.\frac{\partial \phi_{1r}^k}{\partial n}\right|_{\text{tip } Z} \end{bmatrix}$$

$$= \begin{bmatrix} r_2(\boldsymbol{\omega} \times \mathbf{e}) \cdot \mathbf{n}_{\text{tip } 1} \\ \vdots \\ r_2(\boldsymbol{\omega} \times \mathbf{e}) \cdot \mathbf{n}_{\text{tip } Z} \end{bmatrix} \tag{48}$$

The components $\partial \phi_i^k / \partial n$ have been known from the calculation of the zeroth-order flow field whereas the components $\partial \phi_{1r}^k / \partial n$ must be computed at each time step, to account for the new impeller–volute configuration. In order to incorporate the right-hand term in equation (39), the convection scheme in the unsteady first-order solution procedure is extended with an additional operation. At each nodal point the potential jump is updated according to

$$f_{w1}^k = f_{w1}^{k-1} - \overline{w}_{1s} \cdot (w_0^+ - w_0^-) \cdot \Delta t \tag{49}$$

The first-order calculation is repeated until $\phi_1(t) - \phi_1(t - T_1)$ have been converged to the desired accuracy. The time period T_1 of the first-order flow field is defined by

$$T_1 = NT_0 \tag{50}$$

where N is the number of blade pitches defined as the smallest value that satisfies

$$\frac{N\omega}{Z\Omega} \in \mathbb{N}^+ \tag{51}$$

in which $\mathbb{N}^+$ represents the set of positive natural numbers.

After a converged first-order solution has been obtained, the velocity distribution is calculated from equation (34).

7. FLUID FORCES ON THE IMPELLER

The lateral fluid forces on the impeller are computed by applying the law of conservation of momentum to a control surface containing the impeller. The advantage of this method over the direct pressure integration over the blade surfaces is that singularities at the sharp leading edges only slightly affect the accuracy of the calculation of the impeller forces. A control surface fixed to the impeller is chosen in the impeller region as shown in Figure 8.

The instantaneous radial force on the control surface A is defined by

$$\mathbf{F}_c = \frac{\mathrm{D}\mathbf{I}}{\mathrm{D}t} \tag{52}$$

where $\mathbf{I}$ is the linear momentum vector of the fluid inside the control surface,

$$\mathbf{I} = \rho \iint_A b\mathbf{v}\,\mathrm{d}A \tag{53}$$

The material time derivative of $\mathbf{I}$ in equation (52) can be expressed in terms of the local time derivative by using the Reynolds transport equation[14]

$$\frac{\mathrm{D}\mathbf{I}}{\mathrm{D}t} = \frac{\partial \mathbf{I}}{\partial t} + \rho \oint_S \mathbf{b}v(\mathbf{w}\cdot\mathbf{n})\,\mathrm{d}s \tag{54}$$

where S represents the boundary contour of A with outward normal vector $\mathbf{n}$. The resultant force $\mathbf{F}_c$ on the control surface is composed of the pressure force $\mathbf{F}_p$ acting on the boundary contour S_{i0} (in Figure 8 indicated by the dashed curve) and the impeller force denoted by $(-\mathbf{F})$ acting on the fluid inside the control surface. Thus the fluid force on the impeller is

$$\mathbf{F} = \mathbf{F}_p - \mathbf{F}_c \tag{55}$$

where

$$\mathbf{F}_p = -\oint_{S_{i0}} bp\mathbf{n}\,\mathrm{d}s \tag{56}$$

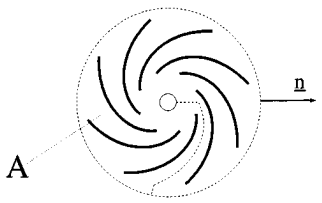

Figure 8. Control surface for the calculation of the impeller forces

Substituting equations (52), (54) and (56) in equation (55) and taking into account that $(\mathbf{w}\cdot\mathbf{n}) = \mathbf{0}$ on the impeller blade surfaces, we find

$$\mathbf{F} = -\frac{\partial \mathbf{I}}{\partial t} - \rho \oint_{S_{i0}} b\mathbf{v}(\mathbf{w}\cdot\mathbf{n})\,\mathrm{d}s - \oint_{S_{i0}} bp\mathbf{n}\,\mathrm{d}s \tag{57}$$

Analogously, we can derive an expression for the shaft moment M by applying the law of conservation of angular momentum to the same control surface

$$M = -\frac{\partial J_z}{\partial t} - \rho \oint_{S_{i0}} b(\mathbf{r}\times\mathbf{v})_z\,(\mathbf{w}\cdot\mathbf{n})\,\mathrm{d}s - \oint_{S_{i0}} bp(\mathbf{r}\times\mathbf{n})_z\,\mathrm{d}s \tag{58}$$

where the z-component of the angular momentum J_z of the fluid inside the control surface is

$$J_z = \rho \iint_A b(\mathbf{r}\times\mathbf{v})\,\mathrm{d}A \tag{59}$$

Note that for a control surface bounded by circles the last term in equation (58) vanishes.

Substituting equations (25a) and (25b) into equation (57) and equating coefficients of equal powers of $(\varepsilon/r_2)^0$ and $(\varepsilon/r_2)^1$ yield the equations for the zeroth-order and first-order forces. For the zeroth-order forces, we have

$$\mathbf{F}_0 = -\frac{\partial \mathbf{I}_0}{\partial t} - \rho \oint_{S_{i0}} b\mathbf{v}_0(\mathbf{w}_0\cdot\mathbf{n})\,\mathrm{d}s - \oint_{S_{i0}} bp_0\mathbf{n}\,\mathrm{d}s \tag{60}$$

where

$$\mathbf{I}_0 = \rho \iint_A b\mathbf{v}_0\,\mathrm{d}A \tag{61}$$

At off-design conditions the zeroth-order forces can have significant unsteady components at the blade passing frequency. The time-averaged values of these forces (averaged over the time period T_0 for one pitch of rotation) are commonly referred to as the radial impeller force.

The first-order forces are given by

$$\mathbf{F}_1 = -\frac{\partial \mathbf{I}_1}{\partial t} - \rho \oint_{S_{i0}} b\mathbf{v}_0(\mathbf{w}_1\cdot\mathbf{n})\,\mathrm{d}s - \rho \oint_{S_{i0}} b\mathbf{v}_1(\mathbf{w}_0\cdot\mathbf{n})\,\mathrm{d}s - \oint_{S_{i0}} bp_1\mathbf{n}\,\mathrm{d}s \tag{62}$$

where

$$\mathbf{I}_1 = \rho \iint_A b\mathbf{v}_1\,\mathrm{d}A \tag{63}$$

The first-order fluid force $\mathbf{F}_1$ is usually resolved into components normal and tangential to the whirl orbit as shown in Figure 9. The normal force component F_{1n} is perpendicular to the whirl orbit and is directed radially outward when positive. The tangential force component F_{1t} acts parallel to the the whirl orbit and is positive when in the direction of the whirl motion of the shaft centre O'. A positive normal force tends to increase the displacement of the impeller. The tangential component F_{1t} has a special meaning in rotor dynamics. In a positive whirl ($\omega > 0$) a positive F_{1t} exerts a destabilising or exciting force, while a negative F_{1t} exerts a stabilising or damping force.

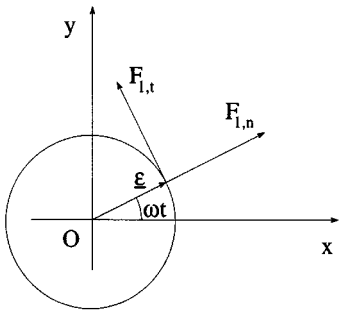

Figure 9. Force components F_{1n} and F_{1t} normal and tangential to the whirl orbit

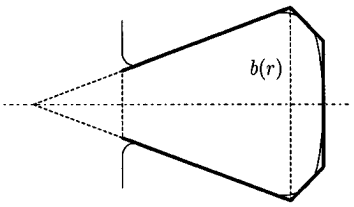

Figure 10. Modelling of volute cross-section. The thin line represents the actual shape and the thick line is the shape used in the analysis

8. RESULTS AND DISCUSSION

In order to validate the finite element model, computations were made on a two-dimensional impeller in a single volute. The configuration considered is that used in the experiments by Arndt and Franz.[3] The impeller Z used in the experiments is a two-dimensional, radial impeller with flat radial shrouds. The hydraulic performance of this impeller is very similar to that of a more complex three-dimensional impeller (referred to as impeller X). Impeller Z is equipped with five logarithmic spiral blades with a blade angle of 25°. Volute A is a conical volute casing with a rounded shape. The approximation for the axial width b is shown in Figure 10. In publications of CalTech[1, 2] volute A is modelled by an 86° logarithmic spiral. However, the cross-sections of volute A (see Appendix II) differ significantly from the logarithmic spiral. For the present computations the dimensions of the volute cross-sections, shown in Appendix II, were used in modelling the volute contour and the axial width function b. The main parameters of the pump geometry and operating conditions are given in Table I. The symbols are explained in Figure 11. The thickness of each blade is one-eighth of the total spacing between the pressure sides of two successive blades, see Figure 12. The blade shape is characterized mathematically by

$$r(\theta) = r_1 \mathrm{e}^{-(\theta-\theta_1)/\tan\beta} \tag{64}$$

where r_1, θ_1 are the co-ordinates of the leading edge. The blade angle β is constant for all radii. The wake curve is modelled as a smooth continuation of the blade suction surface as shown in Figure 12. The wake curve is represented by

$$r(\theta) = r_2 \mathrm{e}^{-(\theta-\theta_2)(1/\tan\beta - c_1)} \left(1 - \frac{\theta-\theta_2}{c_2}\right)^{c_1 c_2} \tag{65}$$

Table I. Geometrical data and operating conditions

Impeller parameters	
Number of blades	$Z = 5$
Blade angle (see Figure 12)	$\beta = 65°$
Radius of leading edge	$r_1 = 0 \cdot 0381$ m
Radius of trailing edge	$r_2 = 0 \cdot 0810$ m
Width in axial direction	$b = 0 \cdot 01575$ m
Volute parameters	
Polar co-ordinates of tongue	$r_t = 0 \cdot 0917$ $\theta_t = -85°$
Operating conditions	
Impeller angular speed	$\Omega = 104 \cdot 72$ rad/s
Optimum volume flow	$Q = 0 \cdot 00584$ m^3/s

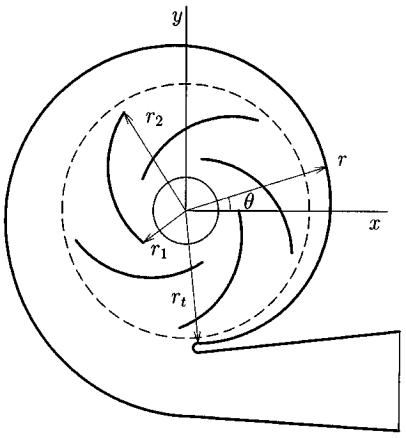

Figure 11. Geometry of impeller Z and volute A

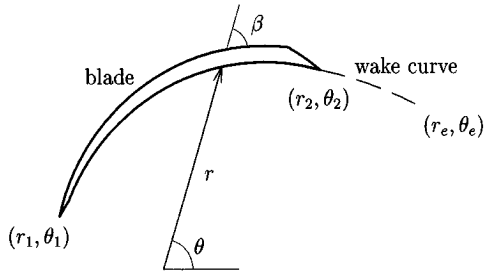

Figure 12. Geometry of impeller blade and wake curve

The constants c_1 and c_2 are determined to match the shape of the average wake curve in a quasi-unsteady analysis. Computations performed with various wake curves showed that changes in the shape and length of the wake curves have no significant influence on the blade circulations.[10]

The algorithm for computing the zeroth- and first-order fluid forces has been implemented in the finite element code Sepran.[15]. Figure 13 shows the two-dimensional finite element mesh of

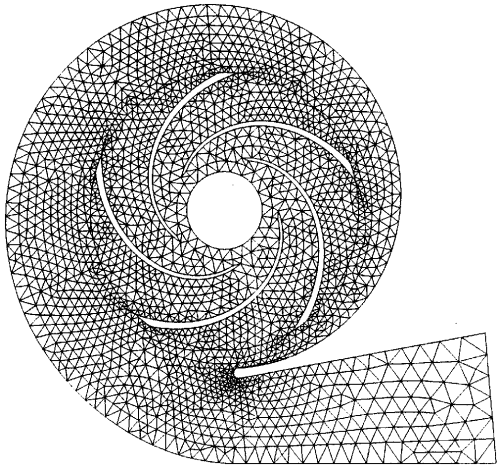

Figure 13. Finite element mesh of impeller Z/volute A

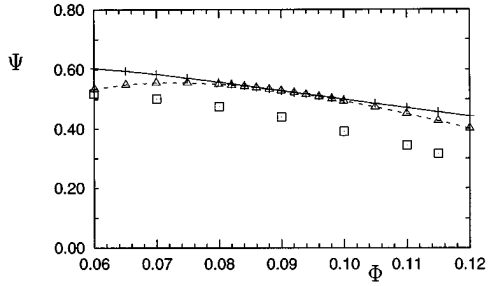

Figure 14. The characteristic of the pump measured (□) and computed numerically using both the quasi-unsteady approach (−−△−−) and the unsteady approach (—)

the impeller–volute configuration. The mesh is refined near the sharp trailing edges of the blades where the Kutta condition is applied. The mesh has 4462 triangular quadratic elements including boundary elements (this amounts to 8935 nodal points). Computations have been performed with 120 elements on the sliding cut. Figure 14 shows the head capacity characteristic of the pump obtained from the numerical calculations. The flow coefficient Φ and the head coefficient Ψ are defined as

$$\Phi = \frac{Q}{2\pi\Omega r_2^2 b} \tag{66}$$

$$\Psi = \frac{gH}{\Omega^2 r_2^2} \tag{67}$$

where H represents the theoretical head rise across the pump according to

$$H = \frac{\bar{M}\Omega}{\rho g Q} \tag{68}$$

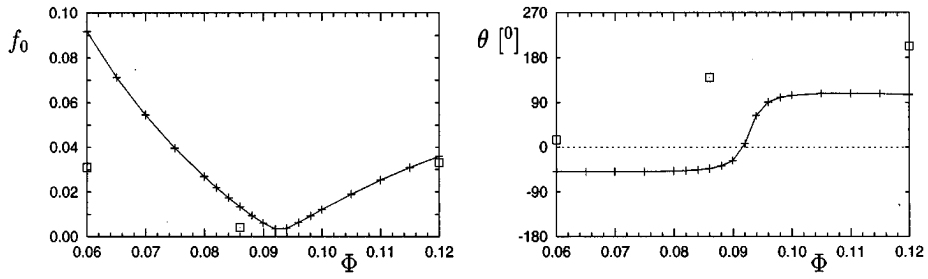

Figure 15. The magnitude and the angle of the average zeroth-order fluid force acting on the impeller using the unsteady approach in the computations (—+—) in comparison with the experimental data (□)

in which the shaft moment M is averaged over the time period T_0. Due to the periodicity of the angular momentum the time average of the time derivative in equation (58) is zero and only the second term contributes to the head. For most values of Φ the computed head is larger than the measured head values presented (approximately 16 per cent for the *best efficiency point*, $\Phi_{BEP} = 0{\cdot}086$). This is due to the use of an inviscid flow model in which dissipative effects in the fluid are neglected. Furthermore, the effects of the discharge-to-suction leakage flow are not included in the flow model. At low flow rates the quasi-unsteady computation predicts a far too small head. This is caused by an overestimation of fluctuations in the blade circulations. When the unsteady wakes are taken into account, these fluctuations are damped and the computation becomes more accurate. A comparison between the experimental and computed steady or averaged radial forces on the impeller is given in Figure 15. The radial impeller force is normalized by

$$\mathbf{f}_0 = \frac{\overline{\mathbf{F}}_0}{\rho\pi\Omega^2 r_2^3 b} \tag{69}$$

where $\overline{\mathbf{F}}_0$ is the zeroth-order force of equation (60) averaged over the time period T_0. Since $\mathbf{I}_0$ and φ_0 are periodic with time T_0, the time-averaged values of the time derivatives $\overline{\partial \mathbf{I}_0/\partial t}$ and $\overline{\partial \varphi_0/\partial t}$ (in p_0) vanish. For a detailed description of the calculation the reader is referred to Reference 16. The magnitude of the computed forces is in qualitative agreement with the measurements, although the computed values are overestimated, particularly for low flow rates. The minimum value of $\mathbf{f}_0$ in the computations is found for $\Phi = 0{\cdot}093$. Based on the two-dimensional potential flow analysis, shock-free entry for impeller Z was found for a flow coefficient $\Phi_s = 0{\cdot}147$. Although the direction of the computed force differs from the experimental values, the change in the direction of the force near the best efficiency point is well predicted. More detailed research, of which the results are not included in this paper, revealed that the excitation forces are very sensitive to the shape of the volute.

In Figure 16 the first-order or rotor-dynamic forces are shown for three flow coefficients, $\Phi = 0{\cdot}060$, $\Phi = 0{\cdot}086$ and $\Phi = 0{\cdot}120$, respectively. In each graph experimental results and forces computed with the quasi-unsteady and with the unsteady approach are shown. The dimensionless force components f_{1n} and f_{1t} are defined by

$$(f_{1n}, f_{1t}) = \frac{(\overline{F}_{1n}, \overline{F}_{1t})}{\rho\pi\Omega^2 r_2^2 b} \tag{70}$$

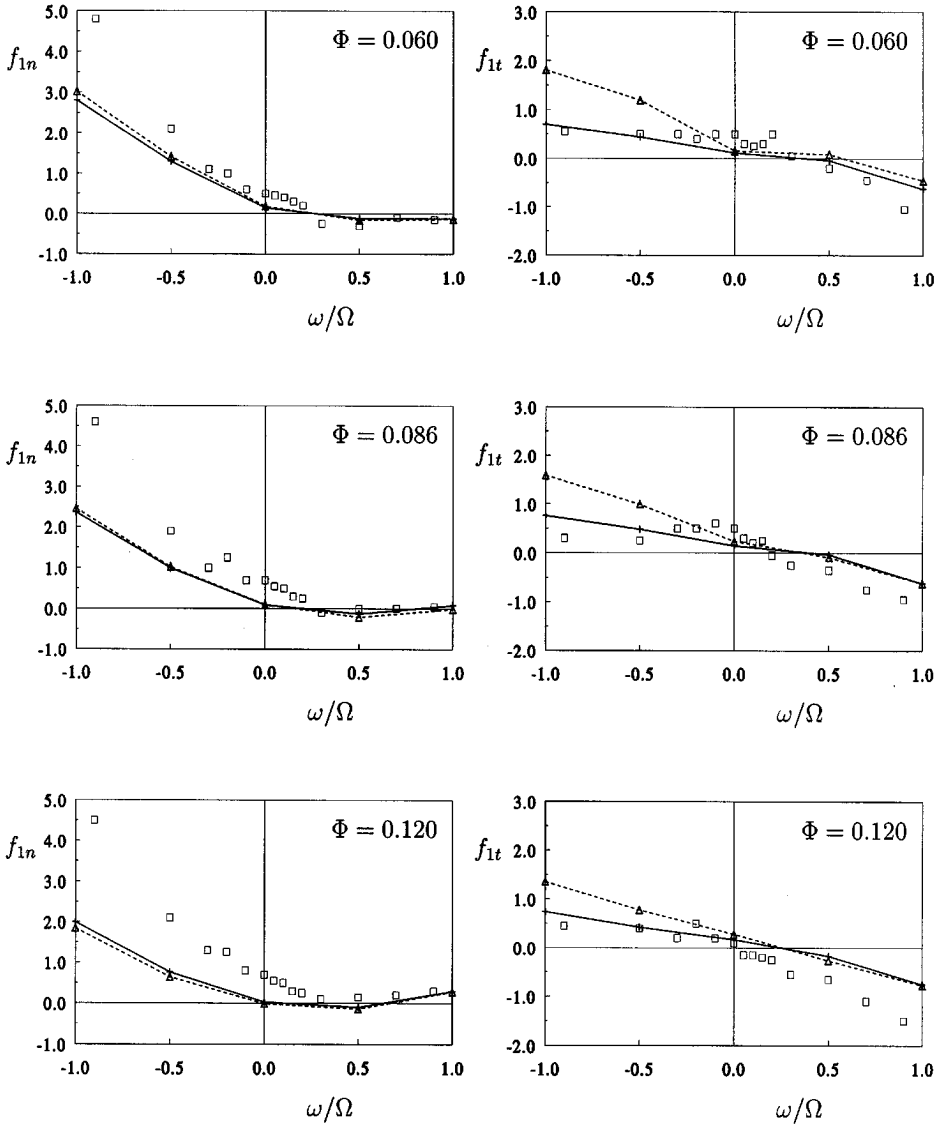

Figure 16. The normal and tangential component of the first-order fluid force acting on the impeller for $\Phi = 0{\cdot}060$, $0{\cdot}086$ and $0{\cdot}120$, respectively. In each graph the forces are plotted computed using the quasi-unsteady approach (––△––) and the unsteady approach (—+—) in comparison with the measured values (□)

where $\overline{F}_{1n}$ and $\overline{F}_{1t}$ are the first-order force components averaged over the time period T_1 of the first-order flow field. The normal forces are approximately parabolic as a function of (ω/Ω), while the tangential forces are approximately linear. For positive whirl ratios $(\omega/\Omega > 0)$ the normal forces are in reasonable agreement with the experimental results. For negative whirl ratios the calculated forces are too small. Note that the normal forces are almost always in the outward direction. The influence of the unsteady wakes is small. Apparently the added mass that is mainly related to the normal force is not changed if wakes are present. The tangential forces calculated

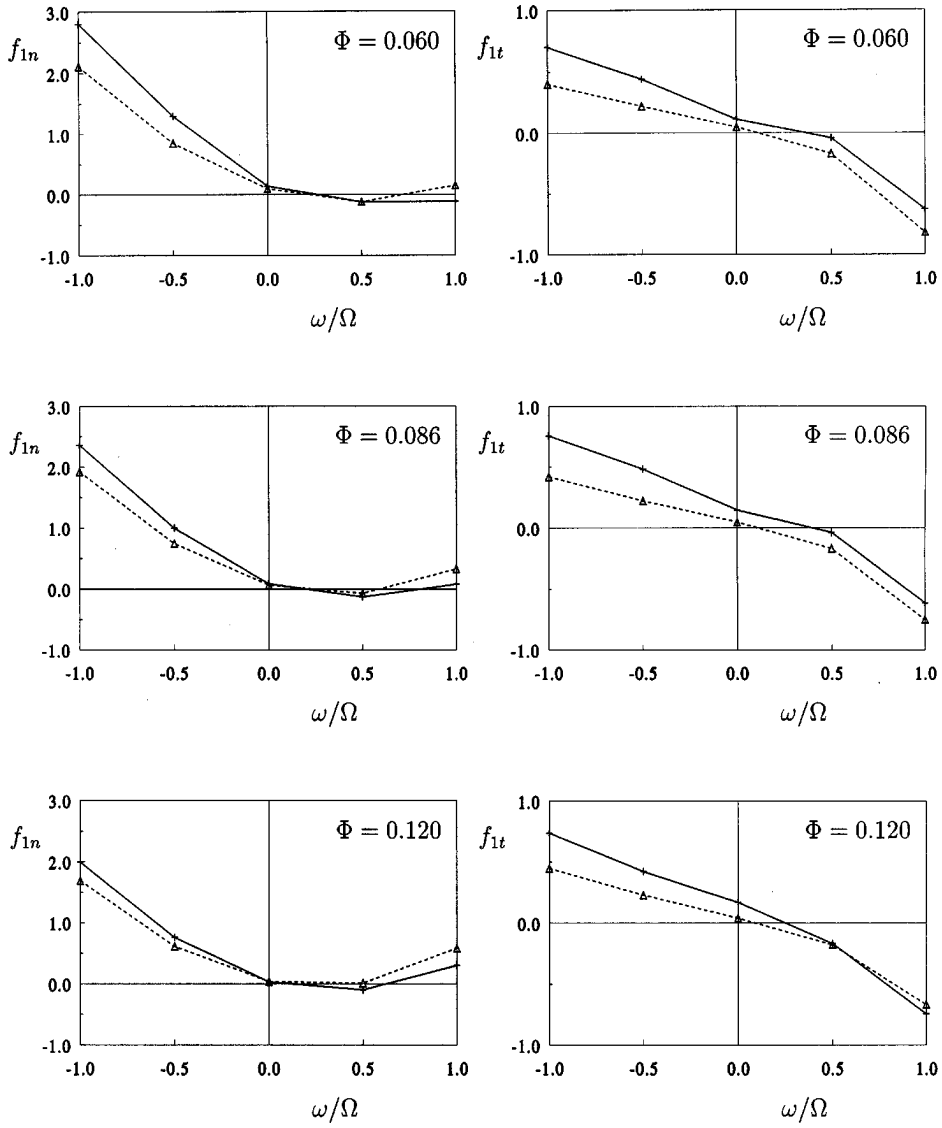

Figure 17. Normal and tangential components of the fluid force acting on the impeller for $\Phi = 0{\cdot}060, 0{\cdot}086$ and $0{\cdot}120$ respectively. In each graph the forces are plotted for the case where the impeller is placed in volute A (—+—) and in the vaneless diffuser (– –△– –)

without unsteady wakes are too large. Better agreement is found when the unsteady wakes are taken into account. The important region of destabilizing tangential forces is predicted fairly well, particularly for small flow rates. In Figure 17, comparisons are made between the results obtained when impeller Z was placed inside volute A, and when the same impeller was placed inside a vaneless diffuser (crudely approximating the case where the impeller is whirling in an infinite medium). In both cases the forces are computed using the unsteady approach. One clearly observes that the region of destabilizing tangential forces is strongly influenced by the presence of the volute

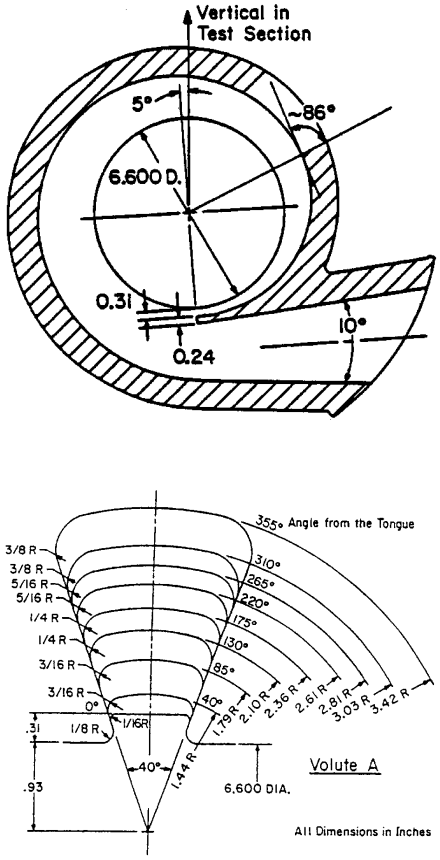

Figure 18. Dimensions of volute A (from Reference 2)

resulting in a much wider destabilizing region ($0 \leqslant \omega/\Omega \leqslant 0{\cdot}4$–$0{\cdot}5$ compared to $0 \leqslant \omega/\Omega \leqslant 0{\cdot}1$ with vaneless diffuser).

9. CONCLUSIONS

A finite element based perturbation method has been developed for computing the lateral fluid forces acting on a centrifugal impeller rotating and whirling in a volute casing. In the analysis the fluid has been assumed to be inviscid and incompressible. The method is applicable to complicated impeller–volute configurations. The numerical results show a good qualitative agreement with the experimental data. The first-order fluid forces have tangential components which damp the whirling motion at most whirl-speed ratios except for the interval $0 < \omega/\Omega < 0{\cdot}4$–$0{\cdot}5$, where a destabilizing effect is observed. This is in agreement with experiments. For the prediction of the important region of destabilizing tangential forces the effect of the volute casing must be incorporated into the model.

ACKNOWLEDGEMENTS

The authors are grateful to J. L. Ammeraal for his assistance in preparing the final manuscript.

APPENDIX I

Moving co-ordinate systems

The material derivative of the velocity potential ϕ is invariant under the transformation from the inertial co-ordinate system (x, y) to the moving system (x', y'), see Figure 1.

$$\frac{\mathrm{D}\phi}{\mathrm{D}t} = \left.\frac{\mathrm{D}\phi}{\mathrm{D}t}\right|' \tag{71}$$

where the superscript $'$ indicates that the derivative is taken in the moving co-ordinate system. In terms of the absolute velocity $\mathbf{v}$ in the Eulerian specification of the flow field, we have

$$\frac{\mathrm{D}\phi}{\mathrm{D}t} = \frac{\partial\phi}{\partial t} + \mathbf{v}\cdot\boldsymbol{\nabla}\phi \tag{72}$$

and in terms of the relative velocity $\mathbf{w}$ (see equation (1)) we have

$$\left.\frac{\mathrm{D}\phi}{\mathrm{D}t}\right|' = \left.\frac{\partial\phi}{\partial t}\right|' + \mathbf{w}\cdot\boldsymbol{\nabla}'\phi \tag{73}$$

The nabla operator is invariant under the transformation from the inertial co-ordinate system to the moving co-ordinate system,

$$\boldsymbol{\nabla}' = \boldsymbol{\nabla} \tag{74}$$

Substituting equations (72-74) into equation (71) gives

$$\frac{\partial\phi}{\partial t} = \left.\frac{\partial\phi}{\partial t}\right|' - (\mathbf{v}-\mathbf{w})\cdot\boldsymbol{\nabla}\phi\ . \tag{75}$$

APPENDIX II

Dimensions of volute A

The dimensions of volute A are illustrated in Figure 18.

REFERENCES

1. D. R. Adkins, 'Analyses of hydrodynamic forces on centrifugal pump impellers', *Ph.D. Thesis*, Division of Engineering and Applied Sciences, California Institute of Technology, 1985.
2. D. R. Adkins and C. E. Brennen, 'Analysis of hydrodynamic radial forces on centrifugal pump impellers', *ASME J. Fluids Eng*., **110,** 20–28 (1988).
3. N. Arndt and R. Franz, 'Measurements of hydrodynamic forces on a two-dimensional impeller and a modified centrifugal pump', *Report no. E249.4*, Division of Engineering and Applied Sciences, California Institute of Technology, 1986.
4. B. Jery, A. J. Acosta, C. E. Brennen and T. K. Caughey, 'Forces on centrifugal pump impellers', *Proc. 2nd Int. Pump Symp*., Houston, Texas, 1985, pp. 21–32.
5. H. Ohashi and H. Shoji, Lateral fluid forces on whirling centrifugal impeller (2nd report: experiment in vaneless diffuser)', *ASME J. Fluids Eng*., **109,** 100–106 (1987).
6. Y. Tsujimoto, A. J. Acosta and C. E. Brennen, 'Theoretical study of fluid forces on a centrifugal impeller rotating and whirling in a volute', *ASME J. Vib. Acoust. Stress Reliability Design*, **110,** 263–269 (1988).
7. W. K. Liu, D. Lam and T. Belytschko, 'Finite element method for hydrodynamic mass with nonstationary fluid', *Comput. Methods Appl. Mech. Eng*., **44,** 177–211 (1984).
8. H. G. Wood and A. A. Thaker, 'Computations of cross coupling stiffness in a whirling pump', *Comput. Methods Appl. Mech. Eng*., **117,** 181–194 (1994).
9. R. Badie, J. B. Jonker and R. A. van den Braembussche, 'Finite element calculations and experimental verification of unsteady potential flow in a centrifugal pump', *Int. j. numer. methods fluids*, **19,** 1083–1102 (1994).

10. T. G. van Essen, 'Fluid-induced impeller forces in centrifugal pumps', *Ph.D. Thesis*, Faculty of Mechanical Engineering, University of Twente, Enschede, The Netherlands, 1995.
11. G. K. Batchelor, *An introduction to Fluid Mechanics*, Cambridge University Press, Cambridge, 1967.
12. R. Badie, 'Analysis of unsteady potential flows in centrifugal pumps', *Ph.D. Thesis*, University of Twente, Enschede, The Netherlands, 1993.
13. D. H. Norrie and G. de Vries, *The Finite Element Method*, American Press, New York, 1973.
14. I. H. Shames, *Mechanics of Fluids*, McGraw-Hill, New York, 1982.
15. A. Segal, *Sepran Manuals: User Manual, Standard Problems and Programmers Guide*, Ingenieursbureau Sepra, Leidschendam, The Netherlands.
16. R. G. K. M. Aarts, 'Pressure calculation in potential flow simulations in a centrifugal impeller in comparison with experimental results', *Report no. WB-ThW/RS-96.029*, University of Twente, Enschede, The Netherlands, 1996.